Clays and Clay Minerals, Vol. 47, No. 5, 605–616, 1999.

ISSN 0009-8604

STRUCTURAL Fe^{3+} IN NATURAL KAOLINITES: NEW INSIGHTS FROM ELECTRON PARAMAGNETIC RESONANCE SPECTRA FITTING AT X AND Q-BAND FREQUENCIES

ETIENNE BALAN,[1] THIERRY ALLARD,[1] BRUNO BOIZOT,[1] GUILLAUME MORIN,[1] AND JEAN-PIERRE MULLER[1,2]

[1] Laboratoire de Minéralogie-Cristallographie, UMR 7590, CNRS, Universités Paris 6 et 7 and IPGP Case 115, 4 Place Jussieu, 75252 Paris Cedex 05, France

[2] IRD, 213 rue Lafayette, 75480 Paris Cedex 10, France

Abstract—Structural Fe^{3+} in kaolinites and dickites covering a broad range of disorder was investigated using electron paramagnetic resonance (EPR) spectroscopy at both the X and Q-band frequencies. A procedure based on a numerical diagonalization of the spin Hamiltonian was used to accurately determine the second and fourth-order fine-structure parameters. A *least-squares* fitting method was also developed to model the EPR spectra of Fe^{3+} ions in disordered local environments, including multimodal site-to-site distributions. Satisfactory fits between calculated and observed X and Q-band spectra were obtained regardless of the stacking order of the samples.

In well-ordered kaolinite, Fe^{3+} ions are equally substituted in sites of axial symmetry ($Fe_{(II)}$ sites, namely $Fe_{(II)a}$ and $Fe_{(II)b}$) which were determined to be the two non-equivalent Al1 and Al2 sites of the kaolinite structure. In dickite, Fe^{3+} ions were also found to be equally substituted for Al^{3+} in the two non-equivalent Al sites of the dickite structure. In poorly ordered kaolinites, the distribution of the fine-structure parameters indicates that Fe^{3+} ions are distributed between $Fe_{(II)}$ sites and other sites with the symmetry of the dickite sites.

Hence, when stacking disorder prevails over local perturbations of the structure, the near isotropic resonance owing to Fe^{3+} ions in rhombically distorted sites ($Fe_{(I)}$ sites) is a diagnostic feature for the occurrence of C-layers in the kaolinite structure, where C refers to a specific distribution of vacant octahedral sites in successive layers.

Key Words—Dickite, Disorder, EPR, Fe^{3+}, Kaolinite.

INTRODUCTION

Kaolinite is a ubiquitous clay mineral at the Earth's surface (Murray, 1988), and one which is known to incorporate defects of various types, either extended (*e.g.*, stacking faults) or localized (*e.g.*, due to impurities). Such defects can often be related to the conditions of genesis of the mineral (Cases *et al.*, 1982; Giese, 1988; Muller *et al.*, 1995). Among the point defects, structural Fe^{3+} is of special importance as iron occurs as the main impurity in all natural kaolinites (Muller and Calas, 1993) and is thought to influence several macroscopic properties, such as the degree of disorder and particle size (*e.g.*, Cases *et al.*, 1982; Giese, 1988).

Due to its high sensitivity, electron paramagnetic resonance (EPR) is probably the most convenient technique for studying both the abundance and distribution of structural Fe^{3+} in kaolinite (*cf.*, Hall, 1980; Muller and Calas, 1993). There has been extensive study of the EPR signal of structural Fe^{3+} in kaolinite (*e.g.*, Goodman and Hall, 1994). X-band EPR spectra show superposed signals, referred to as $Fe_{(I)}$ and $Fe_{(II)}$, interpreted as being due to Fe^{3+} in two types of sites with different degrees of distortion (Meads and Malden, 1975; Angel and Vincent, 1978; Brindley *et al.*, 1986). The $Fe_{(II)}$ signal was recently demonstrated to correspond to Fe^{3+} substituted for Al^{3+} at two non-equivalent, axially distorted octahedral sites (Al1 and Al2) in the kaolinite structure (Gaite *et al.*, 1993). In contrast, no satisfactory structural model has been proposed for the $Fe_{(I)}$ signal corresponding to Fe^{3+} ions in sites having a maximum rhombic distortion. The relative contribution of both types of signal was shown to be related to kaolinite stacking order (*e.g.*, Herbillon *et al.*, 1976; Mestdagh *et al.*, 1982; Brindley *et al.*, 1986; Muller and Bocquier, 1987) or mean coherent domain size (Muller and Calas, 1993): the $Fe_{(II)}$ signal is the most intense in well-ordered kaolinites, whereas the $Fe_{(I)}$ signal is the most intense in poorly ordered samples. Also, the $Fe_{(I)}$ signal may originate from local perturbations around structural Fe^{3+} ions, including perturbations from radiation damage (Gaite *et al.*, 1997). The work of Bonnin *et al.* (1982) suggested that a continuous site-to-site distribution of the crystal field around Fe^{3+} is more appropriate than a simple two-site model for calculating the $Fe_{(I)}$ EPR signal, although the approximations used hindered a full understanding of this signal.

The purpose of this paper is to better characterize the location of structural Fe^{3+} within the kaolinite structure and to clarify the relationship between the crystal field symmetry around Fe^{3+} and the structural order of natural kaolinites. Hence, an accurate characterization of crystal field parameters around Fe^{3+}

Table 1. Characterization of kaolinites (DCV, GB3, A1, FU7, and B4) and dickites (SC and MEX). (1) Hydrothermal; (2) Sediment; (3) Soil; Ancillary minerals: Q = quartz; A = anatase; M = mica; G = gibbsite; wt. % Fe_2O_3 = iron content in the raw and DCB-treated samples; R2 = XRD disorder index of Liétard (Cases *et al.*, 1982); $E_{120\ K}$ = EPR disorder index (Gaite *et al.*, 1997) measured at 120 K.

Sample	Reference or source	Locality	Anc. miner.	% wt. Fe_2O_3	R2	E_{120K}
DCV >2 μm	Gaite *et al.*, 1993	Aveyron (1) (France)	—	—	1.35	3.1
				0.25[1]		
GB3	Cases *et al.*, 1982	Cornwall (1) (GB)	M. Q.	0.57	1.09	7.0
				0.53[1]		
A1 <20 μm	Lucas *et al.*, 1987	Manaus (2) (Brazil)	—	—	0.70	9.3
				0.89[1]		
B4 <20 μm	Lucas *et al.*, 1987	Manaus (3) (Brazil)	G. A.	—	0.23	12.6
				0.78[1]		
U7	Cases *et al.*, 1982	Charentes (2) (France)	Q. A.	0.98	0.23	14.0
				0.79[1]		
SC	WARD's	Pennsylvania (USA)	—	0.082	—	—
MEX	WARD's	San Juanito (Mexico)	—	0.025	—	—

[1] DCB-treated samples.

was performed by fitting the EPR spectra at X and Q-band frequencies. As the existence of C-layers in disordered kaolinites was proposed previously (Brindley *et al.*, 1986; Prost *et al.*, 1989), dickite samples were also investigated to test the possible influence of C-layers on the Fe^{3+} spectra of kaolinite. Kaolinite and dickite differ primarily in the distribution of vacant octahedral sites in successive layers, where kaolinite has every layer consisting of B-type layers and dickite alternately has B- and C-layers.

MATERIALS AND METHODS

Samples

Five natural kaolinite samples were selected from hydrothermal alteration, diagenesis, and pedogenesis deposits (Muller and Calas, 1993). These samples are listed in Table 1 together with their sources, mineralogy, and indices relating to structural order. Two samples (DCV and GB3) were recently the subject of detailed EPR investigation (*e.g.*, Gaite *et al.*, 1993, 1997; Allard and Muller, 1998).

The kaolinite content of the samples varied from ~97% (B4) to near 100% (DCV; references in Table 1). Other minerals present consisted mainly of muscovite, quartz, and Al, Fe, or Ti oxides. Selected grain-sizes were used to eliminate most of these accessory phases and to produce homogeneous samples (*e.g.*, DCV) for analysis. The EPR E-index (Gaite *et al.*, 1997) is defined from the width of selected EPR lines and accounts for the stacking disorder as well as for local perturbations related to the presence of point defects. The X-ray diffraction (XRD) R2-index (Cases *et al.*, 1982; Gaite *et al.*, 1997), based on the variations in the (201, 131) band, only accounts for stacking disorder. A comparison of E and R2 values (Table 1) with those of Gaite *et al.* (1997) shows that the selected samples are representative of the widest range of stacking order. Sample DCV is characterized by a low E value and high R2 value. This exceptionally well-ordered kaolinite is the ordered end-member of these samples. In contrast, the FU7 and B4 samples are very poorly ordered kaolinites, which are characterized by low R2 values and high E values.

Two dickite samples from WARD's Natural Science Establishment Inc. were selected. Sample SC is from St. Claire, Pennsylvania, USA. This well-ordered dickite was used by Bish and Johnston (1993) for a structure refinement from powder neutron-diffraction data. Another sample (MEX) is from San Juanito, Mexico.

EPR spectroscopy

Data acquisition. EPR measurements were performed using a Bruker ESP300E spectrometer, at both the 9.42 GHz (X-band) and 34.0 GHz (Q-band) frequencies. The EPR spectra were recorded at 120 K, using a cooled nitrogen flow device. Owing to exceptional resolution of the EPR spectra for the DCV end-member and dickite samples, measurements were also performed at ambient temperature, and an X-band spectrum was recorded at 4 K for DCV. At low-temperature, the EPR signal owing to paramagnetic centers was enhanced with respect to the broad baseline signal assigned to residual superparamagnetic iron-oxides (Bonnin *et al.*, 1982; Clozel *et al.*, 1994). Calibrated silica tubes (suprasil grade) were filled with dry powdered sample prior to analysis.

The experimental parameters were as follows: 100 kHz frequency modulation and 40 mW microwave power for both X and Q-band; 5×10^{-4} and 10^{-3} T modulation amplitude for X and Q-band, respectively. The EPR spectra were recorded in the 0–0.4 and 0–1.6 T magnetic field range for X and Q-band measurements, respectively. Magnetic field calibration was performed with the DPPH standard ($g = 2.0037 \pm 0.0002$). Frequency calibration was precisely achieved using a Hewlett Packard frequency meter.

Baseline correction of EPR spectra. Iron oxides are always associated with natural kaolinites (Malengreau *et al.*, 1994). These oxides are responsible for a broad resonance ($\Delta H > 0.1$ T) which is superposed on the EPR signal for kaolinite wherever the oxides occur as distinct phases or as coatings (Angel and Vincent, 1978; Bonnin *et al.*, 1982). For this reason, Fe oxides were eliminated prior to analysis using the dithionite-citrate-bicarbonate (DCB) method (Mehra and Jackson, 1960), which has no apparent influence on the kaolinite structure or the shape and the intensity of the EPR signals of paramagnetic species (Muller and Calas, 1989). After this treatment, the residual signal owing to Fe-oxides was sufficiently weak to be neglected in the DCV sample. For the other samples, a broad isotropic signal remained due to residual nanocrystalline, superparamagnetic iron oxide species (Muller and Calas, 1993), although the intensity of the peak was reduced at low temperature. The contribution of this signal was subtracted using a spline function adjusted on selected points, *i.e.*, between paramagnetic lines. For the FU7 and B4 samples, for which paramagnetic Fe^{3+} lines are broad, a trial-and-error procedure was used until the best fit of the spectra was obtained (see below).

Parameter refinement. The fine-structure parameters from the X-band and Q-band EPR powder spectra were determined using the calculation procedure of Morin and Bonnin (1999) based on a numerical diagonalization of the classical spin Hamiltonian (Abragam and Bleaney, 1970):

$$\mathbf{H} = \underbrace{\beta \boldsymbol{H} \boldsymbol{g} \boldsymbol{S}}_{\text{Zeeman Term}} + \underbrace{\sum_{n=2,4} \sum_{m=-n}^{n} B_n^m O_n^m}_{\text{Fine Structure Term}} \qquad (1)$$

where $\beta = 9.27 \times 10^{-23}$ JT^{-1} is the Bohr magneton; $\boldsymbol{g}$ is the gyromagnetic tensor; $\boldsymbol{H}$ is the magnetic field vector; $\boldsymbol{S}$ is the spin operator; O_n^m are the conventional Stevens operators (Abragam and Bleaney, 1970; Buckmaster, 1962; Rudowicz, 1985) and B_n^m are the corresponding fine-structure parameters. The Stevens operators are related to the indirect effects of the crystal field on the spin levels of the paramagnetic ion and thus reflect the local symmetry of the crystal field. For Fe^{3+} ions, the gyromagnetic tensor of the Zeeman term is nearly isotropic, with a mean $\boldsymbol{g}$ value equal to 2, and the fine-structure terms of the Hamiltonian are written using second and fourth-order Stevens operators (Abragam and Bleaney, 1970).

The numerical diagonalization of the spin Hamiltonian allows an accurate determination of the Fe^{3+} spin transitions. These transitions can be characterized by their magnetic field positions and transition probabilities as a function of the spatial orientation of the magnetic field vector with respect to the crystal field tensor principal axes. Energy levels are sorted in ascending order and designated as (1,2, ... 6) for convenience. Transitions are indexed to the corresponding energy levels and magnetic field orientation. For example, 23X corresponds to the transition between levels 2 and 3 when the magnetic field vector lies along the X axis and 23XY is the same transition when the magnetic field vector lies in the XY plane but not on the X or Y axis. Due to the possible crossing of energy levels, transitions may appear several times between the same energy levels for a given orientation. Consequently, a third number is used to specify the order of appearance of the transition within the magnetic field range of measurement, *e.g.*, 230X for the first appearance of the 23 transition along the X axis. The EPR powder-absorbance spectrum is computed by summing the contribution of each of the orientations of the magnetic field vector with respect to the reference frame. The classical first derivative EPR spectrum is computed by convoluting the calculated absorbance spectrum with a first derivative Lorentzian function. The fine-structure parameters of the Fe^{3+} sites are determined by fitting the positions of the transitions, with indexing achieved by comparing calculated and experimental spectra (Morin and Bonnin, 1999).

Inversion procedure for EPR spectra of disordered materials. Disordered materials exhibit broad EPR spectra which can be interpreted as the result of large and nearly continuous variations of fine-structure parameters (Kliava, 1986). Therefore, such EPR spectra cannot be interpreted using only one set of fine-structure parameters. Studies using parameterized distributions have been used successfully to model the EPR spectra of Cr^{3+} and Fe^{3+} in glasses (Legein *et al.*, 1995). A crystal field distribution was also proposed for the interpretation of the X-band EPR spectra of kaolinites (Bonnin *et al.*, 1982), but this approach was of limited utility because it was restricted to the distribution of the rhombicity parameter, *i.e.*, the ratio of second-order fine-structure parameters ($\lambda = B_2^2/B_2^0$). In the present study, the two-dimensional distribution of both B_2^0 and B_2^2 parameters are determined to extract information regarding the site-to-site variations of the crystal field around Fe^{3+} ions. This approach, which does not require a preliminary analytical expression of the distribution of the fine-structure parameters, is explained as follows.

The EPR spectrum $\Pi(H)$ of any disordered solid, *i.e.*, a solid which presents a broad site-to-site variation of the fine-structure parameters, can be described by the following equation (Equation 2.21 from Kliava, 1986):

$$\Pi(H) = 1/4\pi \int_\theta \int_\varphi \int_{B_n^m} P(B_n^m) W(B_n^m, \theta, \varphi, H) \times F(B_n^m, \theta, \varphi, H) \sin(\theta)\, d\theta\, d\varphi\, dB_n^m \qquad (2)$$

where H is the magnetic field value, $P(B_n^m)$ is the density of probability of the spin Hamiltonian parameters,

$W(B_n^m, \theta, \varsigma, H)$ is the transition probability, $F(B_n^m, \theta, \varsigma, H)$ is the lineshape function, and θ and ς are the azimuthal and polar angles defining the orientation of the magnetic field vector. The triple integration is performed over all possible orientations of the magnetic field and over the distributed values of spin Hamiltonian parameters. $P(B_n^m)$ may be extracted by applying an approach similar to that used for modeling Mössbauer spectra of iron in glasses (Levitz *et al.*, 1980).

As the fourth-order parameters ($n = 4$) are weaker than the second-order parameters (Gaite *et al.*, 1993), they can be neglected in Equation (2). The integration over the fine-structure parameters may be thus approximated with a summation over discrete values of B_2^0 and B_2^2. This results in the following expression:

$$\Pi(H) = \sum_{B_2^0} \sum_{B_2^2} P(B_2^0, B_2^2) \times \int_0 \int_\varphi (1/4\pi W(B_2^0, B_2^2, \theta, \varphi, H) \times F(B_2^0, B_2^2, \theta, \varphi, H)) \sin(\theta)\, d\theta\, d\varphi \quad (3)$$

where $P(B_2^0, B_2^2)$ is the two-dimensional distribution of the second-order fine-structure parameters.

Equation (3) can be simplified by the fact that the integral on the right side of this equation is the expression of the spectrum resulting from one set of fine-structure parameters (B_2^0, B_2^2):

$$\Pi(H) = \sum_{B_2^0} \sum_{B_2^2} P(B_2^0, B_2^2) C(B_2^0, B_2^2, H) \quad (4)$$

where $C(B_2^0, B_2^2, H)$ is the intensity of the calculated spectrum at field H, for a given (B_2^0, B_2^2) couple.

The EPR spectrum is recorded as a set of $\Pi_e(H_i)$ values obtained for discrete values of magnetic field H_i. A system of equations is obtained by writing Equation (4) for any values of magnetic field. This system of equations can be written in the form

$$\boldsymbol{E} = \boldsymbol{CX} \quad (5)$$

where $\boldsymbol{E}$ is a column vector containing the measured data values $\Pi_e(H_i)$. $\boldsymbol{C}$ is a matrix such that each column vector corresponds to the calculated spectrum $C(B_2^0, B_2^2, H)$ for a (B_2^0, B_2^2) couple, each row corresponding to an H_i value. Finally, $\boldsymbol{X}$ is a column vector containing the $P(B_2^0, B_2^2)$ values. These values are determined by solving Equation (5) by minimizing the quantity

$$(\boldsymbol{E} - \boldsymbol{CX})^2 \quad (6)$$

which is equivalent to minimizing the quantity

$${}^t\boldsymbol{X}{}^t\boldsymbol{CCX} - 2{}^t\boldsymbol{X}{}^t\boldsymbol{CE} \quad (7)$$

where the superscript, t, refers to the transposed matrix.

The $\boldsymbol{C}$ matrix is defined over a triangular lattice of B_2^0 and B_2^2 parameters with the convention that $B_2^0 \geq B_2^2$ and with the implicit assumption that $P(B_2^0, B_2^2)$ is equal to zero beyond this area. Numerical testing allowed us to eliminate B_2^0 values >0.15 cm^{-1} for the EPR spectra of Fe^{3+} in kaolinites. A B_2^m step of 0.005 cm^{-1} was used to maintain the matrix sizes and the computation time within practicable ranges. Initial calculations based on the X-band data gave a noisy unreliable distribution of fine-structure parameters because the column vectors of the $\boldsymbol{C}$ matrix at X-band frequency may be collinear when $B_2^0 \approx B_2^2$. A reliable distribution was obtained by performing calculations simultaneously on both X and Q-band EPR data.

Additionally, two types of physically meaningful constraints were introduced in the fitting procedure. First, the quadratic programming routine EO4NAF from the FORTRAN NAG library was used during the *least-squares* minimization to keep the $P(B_2^0, B_2^2)$ values positive. Second, smoothing of the $P(B_2^0, B_2^2)$ distribution was achieved by minimizing its second derivatives, expressed as two matrix $\boldsymbol{F}_1$ and $\boldsymbol{F}_2$, as defined in Levitz *et al.* (1980).

Consequently, $P(B_2^0, B_2^2)$ values can be determined by minimizing the following quantity:

$${}^t\boldsymbol{X}({}^t\boldsymbol{C}_x\boldsymbol{C}_x + \gamma{}^t\boldsymbol{C}_q\boldsymbol{C}_q + \alpha_1\boldsymbol{F}_1 + \alpha_2\boldsymbol{F}_2)\boldsymbol{X} - 2{}^t\boldsymbol{X}({}^t\boldsymbol{C}_x\boldsymbol{E}_x + \gamma\chi{}^t\boldsymbol{C}_q\boldsymbol{E}_q) \quad (8)$$

where the x and q indices correspond to X and Q-band respectively, α_1 and α_2 are numerical constants which are chosen such that both the smoothness of $P(B_2^0, B_2^2)$ and the fit of the experimental data are acceptable, χ is a scale factor applied to the Q-band spectrum and γ is a numerical constant which allows a weighting of the Q-band versus the X-band data. The χ value is calculated using an iterative process.

RESULTS

X and Q-band EPR spectra description

As expected (*e.g.*, Muller and Calas, 1993; Clozel *et al.*, 1994), two groups of signals were observed in the X-band EPR spectra of the kaolinites analyzed (Figure 1). One group, observed at low magnetic field, is due to Fe^{3+} ions in sites with different distortions: (1) the $Fe_{(I)}$ signal, which corresponds to rhombically distorted sites ($\lambda \approx 1$), appears as a nearly isotropic signal centered at 0.16 T; (2) the $Fe_{(II)}$ signal, which corresponds to sites with a more axial distortion ($\lambda \approx 0.65$), consists of an anisotropic signal with resonances near 0.074, 0.136, 0.180, and 0.214 T. Note that the EPR spectrum of DCV exhibits two $Fe_{(II)}$ signals ($Fe_{(II)a}$ and $Fe_{(II)b}$) which are attributed to Fe^{3+} substitutions for Al^{3+} in the two Al sites of the kaolinite structure (Gaite *et al.*, 1993). With increasing disorder, several of these lines cannot be resolved due to line broadening. The second group of signals, centered at 0.33 T, results from an overlay of: (1) a broad resonance ($\Delta H > 0.1$ T) due to superparamagnetic Fe oxides, (2) a sharp, intense signal due to radiation-induced defects

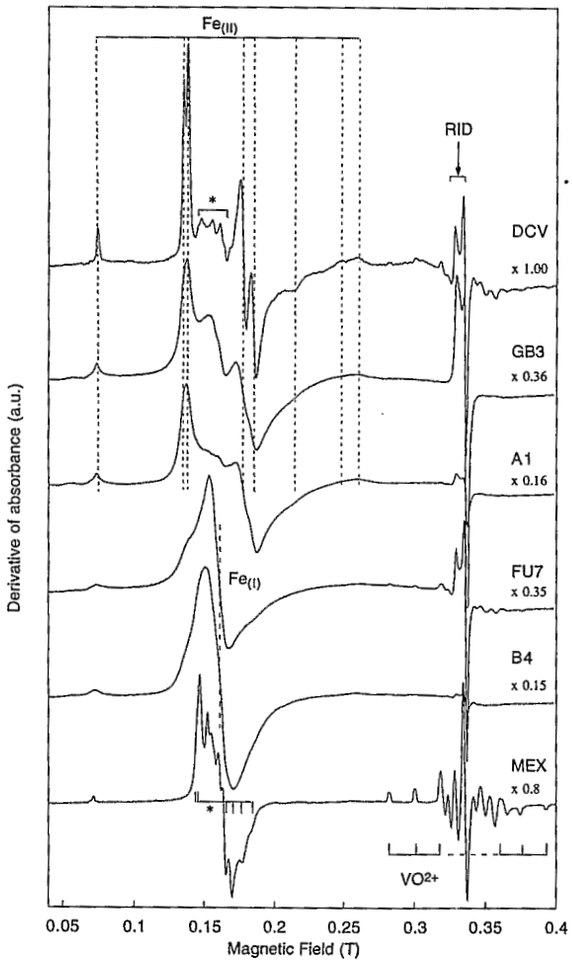

Figure 1. Full range X-band EPR spectra, recorded at 120 K, for kaolinites DCV, GB3, A1, FU7, and B4 and for dickite MEX. The intensity is normalized to the DCV spectrum and the normalization factor is reported. Stacking order for the kaolinites decreases from the top to the bottom of the figure. $Fe_{(I)}$ and $Fe_{(II)}$ = superposed signals at low magnetic field arising from Fe^{3+} ions substituted for Al^{3+} in the two sites of the kaolinite structure; RID = radiation-induced defects (sharp signal at high magnetic field); VO^{2+} = vanadyl ions producing an 8-line hyperfine structure superposed on the RID signal (DCV and FU7 samples). Note the line splitting for resonances centered at 0.136 and 0.180 T on the EPR spectrum of DCV, which indicates the presence of two different $Fe_{(II)}$ sites, referred to as $Fe_{(II)a}$ and $Fe_{(II)b}$. Features indicated by (*) on the DCV and the MEX spectrum correspond to Fe^{3+} centers in dickite and are explained in Figure 6.

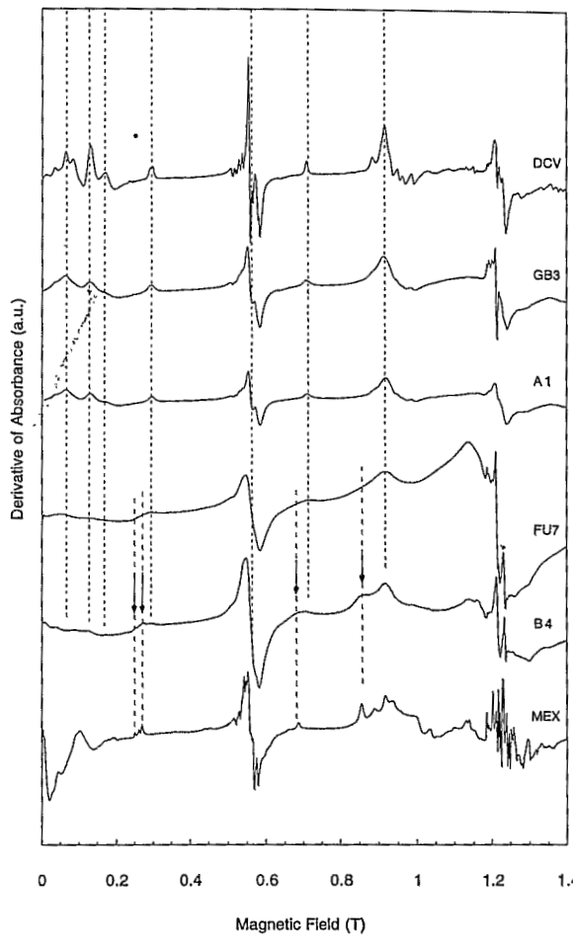

Figure 2. Full range Q-band EPR spectra, recorded at 120 K, for kaolinites DCV, GB3, A1, FU7, and B4 and for dickite MEX. Stacking order for kaolinites decreases from the top to the bottom of the figure. Arrows indicate specific features presented by the EPR spectrum of B4 kaolinite and MEX dickite.

(RIDs), and (3) for two samples (DCV and FU7), additional lines related to the hyperfine structure of vanadyl (VO^{2+}) complexes.

In addition, Figure 1 shows a strong variation of the relative intensities of $Fe_{(I)}$ and $Fe_{(II)}$ signals as a function of stacking order: the well-ordered DCV kaolinite only exhibits the $Fe_{(II)}$ signal whereas the poorly ordered FU7 and B4 kaolinites mainly show a broad (ΔH = 0.02 T), nearly isotropic signal at 0.16 T, *i.e.*, the $Fe_{(I)}$ signal.

Note also in Figure 1 that the signal centered at 0.16 T in the X-band spectrum of the MEX dickite and the $Fe_{(I)}$ signal observed in the X-band spectrum of the B4 kaolinite have a similar shape, although the dickite signal presents more defined lines. As rhombic signals around 1.6 T are very common features of Fe^{3+} spectra in the X-band, caution must be used in interpreting these signals on such a similarity. In contrast, the Q-band spectra should provide less ambiguous information concerning the local symmetry around Fe^{3+}.

The Q-band EPR spectra of the kaolinites and the MEX dickite are presented in Figure 2. Numerous lines occurring at similar positions are observed in the Q-band spectra of the kaolinites. The most intense (dotted lines in Figure 2) are located in the low-field region (0–0.2 T) and at 0.29, 0.57, 0.71, and 0.92 T.

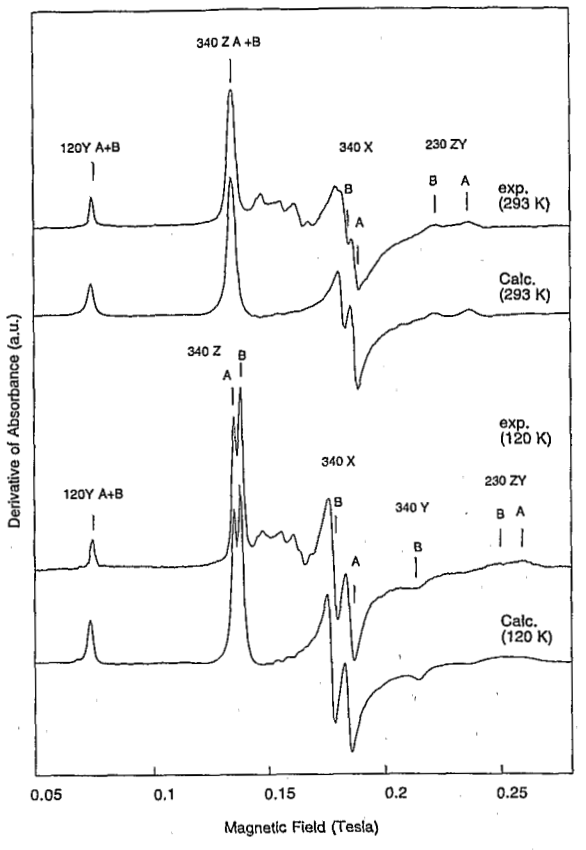

Figure 3. Comparison of the X-band EPR spectra of DCV kaolinite obtained at 293 and 120 K with the calculated spectra. Note that 230ZY transitions are inter-doublet transitions.

Using rough line indexation, Meads and Malden (1975) suggested that these lines are due to three Fe^{3+} sites. We show below that these lines may be assigned to Fe^{3+} ions substituted for Al^{3+} in the kaolinite structure.

In contrast to the X-band spectra, the Q-band spectra cannot be easily interpreted as the superposition of two distinct signals corresponding to the $Fe_{(I)}$ and $Fe_{(II)}$ signals. Indeed, the shapes of the Q-band spectra do not vary drastically between samples; no shift of the main lines is observed for the poorly ordered kaolinites with respect to their position in DCV. An overall increase in line broadening is observed as a function of increasing stacking disorder. The most disordered samples (B4 and FU7) exhibit three additional weak bands at 0.27, 0.68, and 0.87 T (arrows on Figure 2) which may be related to the $Fe_{(I)}$ signal observed on X-band spectra. These features are also observed in the Q-band spectrum of the Mexico dickite. This suggests the occurrence of dickite layers in poorly ordered kaolinites.

In addition to the lines attributed to Fe^{3+} ions, a broad signal caused by the superparamagnetic Fe oxides is observed in the region 1–1.4 T of the Q-band spectra of kaolinites. Superposed on this signal is the sharp signal due to radiation induced defects (RIDs), which is particularly intense for the GB3 and FU7 samples. Hyperfine transitions of VO^{2-} were too weak to be clearly distinguished, except in the MEX spectrum.

Determination of fine-structure parameters for Fe^{3+} in well-ordered samples

Parameter refinement for kaolinite. Gaite *et al.* (1993) showed that the main lines (340Z, 340X, 340Y, and 120Y) of the $Fe_{(II)a}$ and $Fe_{(II)b}$ spectra on the X-band spectrum of well-ordered DCV sample obtained at 120 K may be interpreted using only second-order fine-structure parameters. We attempted to calculate the Q-band EPR spectra of DCV kaolinite at 120 K (calculated spectra not shown), using the second-order parameters calculated by Gaite *et al.* (1993) and those determined directly at the same temperature in this study. Using this approach, the general shape of the experimental spectrum can be reproduced, indicating that the lines of the Q-band spectrum are related to $Fe_{(II)}$ parameters defined by the X-band spectra. However, owing to the improved resolution of the lines, discrepancies were observed for line positions and line splittings between the experimental and the calculated spectra. These discrepancies indicate that fourth-order Stevens operators must be used for correctly modeling the Q-band spectrum. Similar conclusions were made by Morin and Bonnin (1999) from the study of EPR powder spectra of Fe^{3+} in various oxide minerals.

The second and fourth-order parameters were thus refined by simultaneously adjusting ~10 line positions for each site for the X and Q-band data. Refinement was performed in the second-order principal axes frame. Calculated X and Q-band spectra at 120 K are compared to the observed spectra in Figures 3 and 4, respectively. Each calculated spectrum is the sum of the calculated $Fe_{(II)a}$ and $Fe_{(II)b}$ spectra added in the same proportions. The introduction of fourth-order terms resulted in a satisfactory fit between the calculated and the observed spectra. This agreement confirms that the Fe^{3+} ions are equally distributed across both $Fe_{(II)}$ sites. Coupling X and Q-band data in the refinement procedure yields high accuracy (± 0.001 cm^{-1}) for the second-order parameters as evidenced by the correct modeling of the 230ZY lines in the X-band and of the low magnetic field lines (0–0.25 T) in the Q-band. Indeed, these lines are highly sensitive to slight variations in second-order fine-structure parameters as they correspond to inter-doublet transitions.

The rhombicity parameters ($\lambda = B_2^2/B_2^0 = 0.61$ and 0.66, for $Fe_{(II)a}$ and $Fe_{(II)b}$, respectively) based on our data are similar to those determined by Gaite *et al.* (1993) ($\lambda = 0.62$ and 0.67, respectively) from X-band data. However, the B_2^0 and B_2^2 values calculated here differ slightly from those reported by Gaite *et al.*

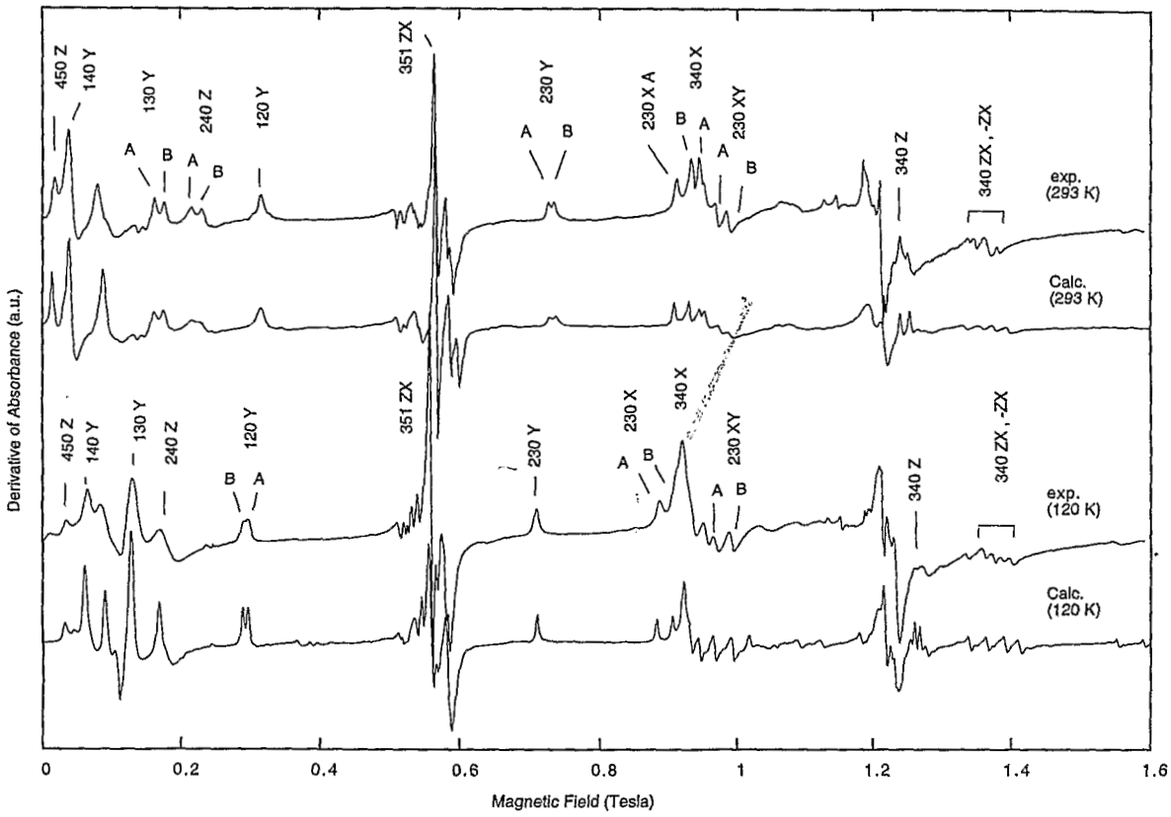

Figure 4. Comparison of the Q-band EPR spectra of DCV kaolinite obtained at 293 and 120 K with the calculated spectra.

(1993) (Table 2). This discrepancy is explained by the introduction of fourth-order parameters in this study, which cannot be determined from X-band data only. The B_4^0 parameter is well constrained because the diagonal O_4^0 Stevens operator has a strong effect on numerous line positions in the Q and X-band. In addition, the position of the 351ZX transition and the splitting of the 340 transition around 1.4 T (Figure 4) indicates high B_4^3 and B_4^{-3} values. The B_4^2 and B_4^4 terms were necessary to match the position of several Q-band lines in the XOY plane, especially the 120Y, 230Y, and 340X lines. The B_4^{-2} and B_4^{-4} terms were used to reproduce the splitting of the angular dependency of the 230 transition in the XOY and −XOY planes. The B_4^1 and B_4^{-1} parameters were not used because they were not constrained sufficiently to be refined. Because Q-band lines arising from A and B-sites overlap frequently (*e.g.*, near 0.92 and 1.2 T), the assignment of 351ZX, 340ZX, and 230XY lines to either site was ambiguous. Despite this ambiguity, the fourth-order parameter values used for spectra calculations are probably of the correct order of magnitude because A and B-sites have very similar spectra. Only accurate and unambiguous determined values, namely B_2^0, B_2^2, and B_4^0, are reported in Table 2.

Table 2. Fine-structure parameters (cm^{-1}) for Fe^{3+} sites in DCV kaolinite at different temperatures.

Temp.	Site	B_2^0	B_2^2	$60 \times B_4^0$
293 K	$Fe_{(II)a}$	0.1104	0.0666	−0.0025
	$Fe_{(II)b}$	0.1057	0.0661	−0.0021
120 K	$Fe_{(II)a}$	0.1156	0.0721	−0.0033
	$Fe_{(II)b}$	0.1120	0.0753	−0.0020
4 K	$Fe_{(II)a}$	0.1198	0.0739	nd.
	$Fe_{(II)b}$	0.1150	0.0768	nd.
120 K[1]	$Fe_{(II)a}$	0.11	0.069	nd.
	$Fe_{(II)b}$	0.12	0.077	nd.

Note: accuracy is ±0.0010 cm^{-1}, nd.: not determined.
[1] Gaite *et al.* (1993).

Gaite *et al.* (1993) showed that the rhombicity parameter of the $Fe_{(II)}$ signals is temperature-dependent. The present study confirms this observation: on Q-band spectra (Figure 4), a lowering of temperature from 293 to 120 K results, for example, in important shifts of the 130Y, 240Z, 120Y, 230Y, 230X, and 340X transitions. Fine-structure parameters were also refined for spectra obtained at 293 K (X and Q-band spectra) and 4 K (X-band spectrum only). Spectra obtained at 293 K and the corresponding calculated spectra are presented in Figures 3 and 4. The refined values of fine-structure parameters are reported in Table 2. Note that the B_2^0 values for $Fe_{(II)a}$ and $Fe_{(II)b}$ sites increase in

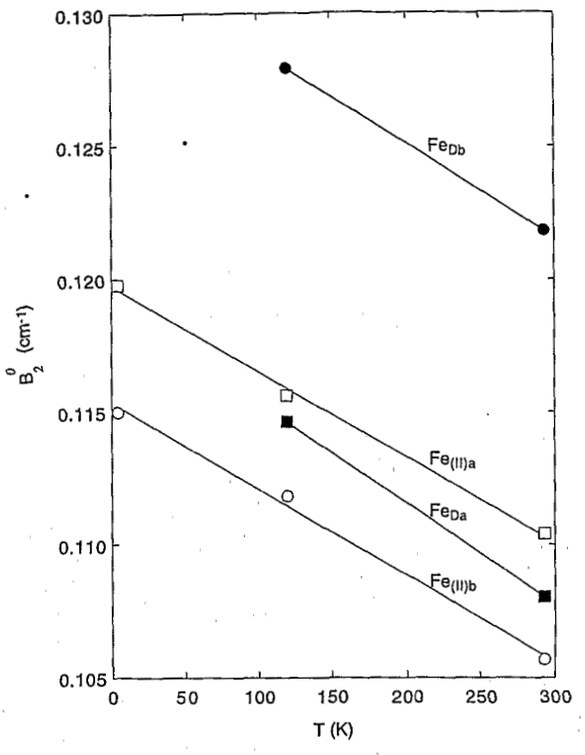

Figure 5. Variation of the experimental B_2^0 parameter (cm^{-1}) for DCV and SC as a function of temperature.

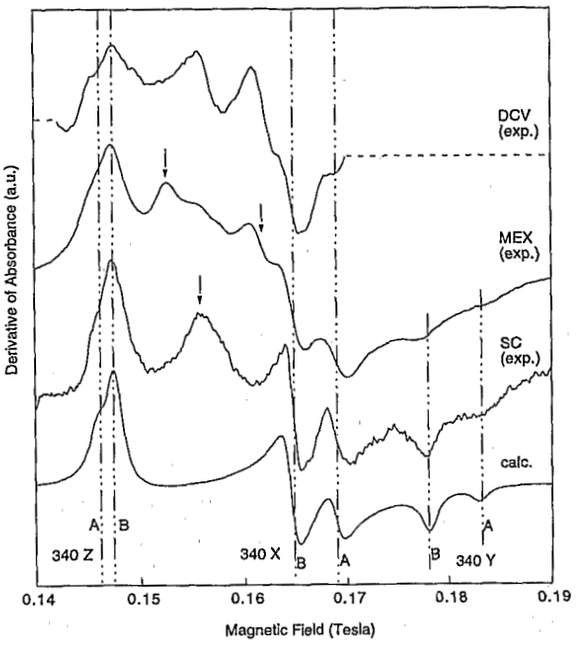

Figure 6. Comparison of the X-band EPR spectra of the two dickite samples (SC and MEX), obtained at 120 K in the region 0.14–0.19 T, and of the DCV kaolinite, obtained at 120 K in the region 0.14–0.17 T, with the calculated spectrum of SC dickite and the corresponding observed spectrum. Note that the two spectra for dickite exhibit six common lines (marked by vertical doted lines), four being also present in the DCV spectra. Arrows indicate unexplained features.

parallel and linearly as a function of decreasing temperature (see Figure 5). A regular increase was also observed for the B_2^2 values, but the variations were not linear.

Parameter refinement for dickite. The X-band EPR spectra of SC and MEX dickite samples obtained at 120 K in the 0.14–0.19 T region are presented in Figure 6. These detailed spectra correspond to the central lines observed around 0.16 T on the full-range X-band spectra of DCV and MEX presented in Figure 1. The X-band spectrum of DCV in the 0.14–0.17 T region is also reproduced for comparison. In this region, the observed lines are attributed unambiguously to Fe^{3+}. The two spectra for dickite exhibit seven common lines. Six of these (vertical dotted lines in Figure 6) are interpreted as resulting from the angular dependencies of the 340 transition of two distinct Fe^{3+} spectra, referred to as Fe_{Da} and Fe_{Db} below. Fine-structure parameters for both sites, refined by adjusting the positions of these lines at both 120 K and room temperature are reported in Table 3 and Figure 5. Fe_D sites in dickite exhibit B_2^0 values close to those determined for the $Fe_{(II)}$ sites in kaolinite. In contrast, the B_2^2 parameters are significantly larger than those determined for kaolinite, the Fe_D sites being more rhombically distorted. Fitting of the experimental X-band spectrum indicates that the Fe_{Db} and Fe_{Da} sites are occupied equally by Fe^{3+}, one signal (Fe_{Da}) being slightly broader than the other. The residual signal [minor lines at 0.158 (MEX, SC), 0.154, and 0.162 T (MEX) indicated by arrows in Figure 6] could not be interpreted from the data.

Five of the lines common to SC and MEX dickite samples are also observed on the spectrum for DCV (Figure 6). They correspond to the weak rhombic signal observed between the main 340Z and 340X $Fe_{(II)}$ lines of the DCV X-band spectra presented in Figure 3 in the present paper and in Figure 3 and 4 in Gaite *et al.* (1993). This provides clear evidence of the occurrence of a minor quantity of ordered dickite in the DCV sample.

Table 3. Fine-structure parameters (cm^{-1}) for Fe^{3+} sites in SC dickite at 120 and 293 K.

Temp.	Site	B_2^0	B_2^2	$60 \times B_4^0$
293 K	Fe_{Da}	0.1084	0.0851	0.0001
	Fe_{Db}	0.1218	0.9926	0.0024
120 K	Fe_{Da}	0.1146	0.0901	−0.0005
	Fe_{Db}	0.1279	0.1031	0.0016

Note: accuracy is ±0.0010 cm^{-1}.

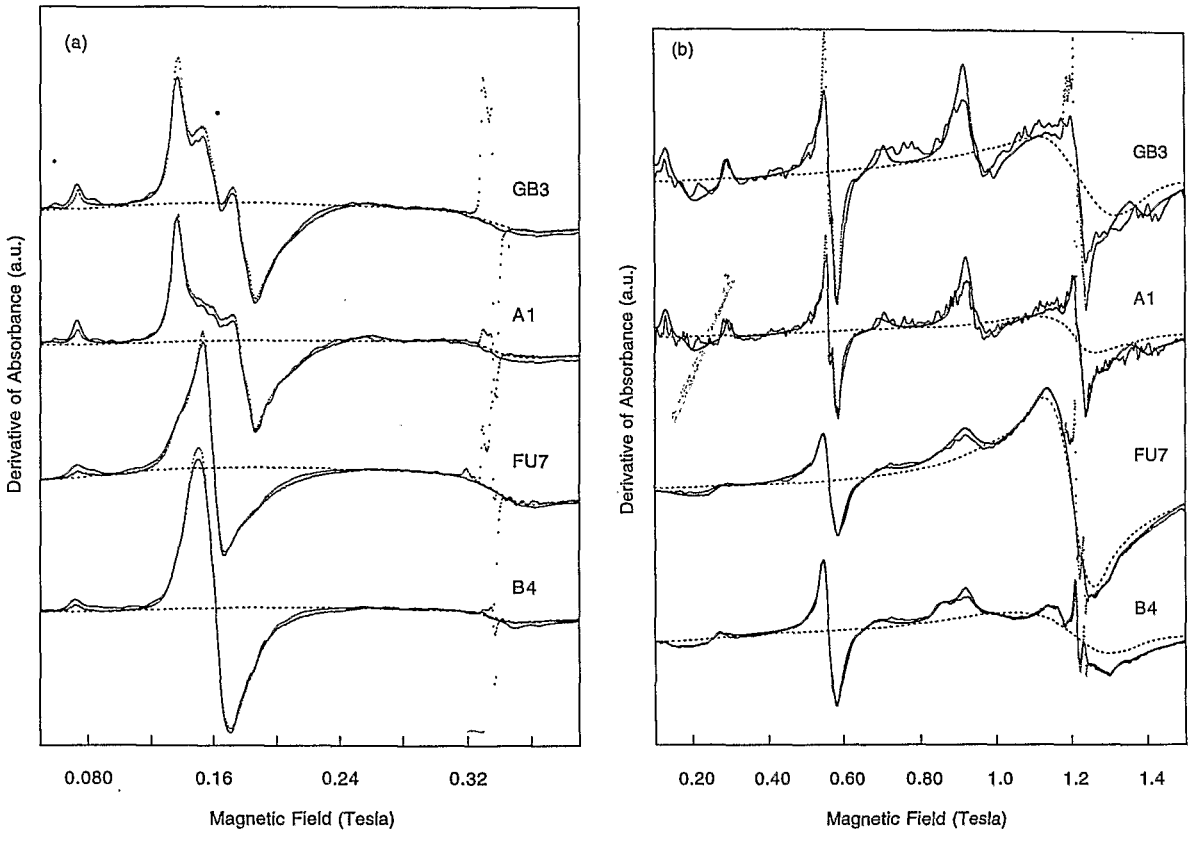

Figure 7. Comparison of X and Q-band spectra, recorded at 120 K, for the variably ordered kaolinites GB3, A1, FU7, and B4 with the spectra calculated using the inversion procedure. Note that satisfactory fits were obtained for the X-band spectra whereas some discrepancies are observed for the Q-band spectra. Points = observed data, continuous line = calculated spectra, dotted line = baseline.

Distribution of fine-structure parameters in poorly ordered samples

The inversion procedure (see methods section) was applied to all the kaolinite samples except DCV to correlate line broadening (see above) with the distribution of fine-structure parameters. In Figure 7, the computed X and Q-band spectra for the GB3 and A1 kaolinites (with $Fe_{(II)}$ signal more intense than the $Fe_{(I)}$ signal) and for FU7 and B4 kaolinites (with a dominant $Fe_{(I)}$ signal) can be compared to the spectra obtained at 120 K. Satisfactory fits between the calculated and the observed X-band spectra (Figure 7a) were obtained, although some discrepancies remained between the calculated and observed Q-band spectra (Figure 7b). These discrepancies are most pronounced for the GB3 and A1 samples which have high stacking order. These discrepancies are due to the limited number of EPR spectra (496 in total for each frequency) used to model the distribution of fine-structure parameters and also to the use of only second-order parameters for EPR spectra computation.

The distributions of fine-structure parameters for GB3, A1, FU7, and B4 are presented in Figure 8. The calculated values for fine-structure parameters are mostly concentrated in a relatively narrow area (0.10 $cm^{-1} \leq B_2^0 \leq 0.13\ cm^{-1}$; 0.06 $cm^{-1} \leq B_2^2 \leq 0.11\ cm^{-1}$). A one-mode distribution around the $Fe_{(II)}$ fine-structure parameters is observed for the ordered GB3 and A1 kaolinites. Note that the maximum of the distribution is systematically shifted relatively to the $Fe_{(II)}$ parameters along an axis of constant rhombicity ($\lambda_K = B_2^2/B_2^0 \approx 0.65$). This shift is attributed to the use of second-order parameters only in the distribution calculation. In contrast, several modes can be distinguished for the poorly ordered FU7 and B4 kaolinites. Three modes are particularly well differentiated for the B4 sample. Two modes are close to the two distinct fine-structure parameter sets calculated for the Fe_{Da} and Fe_{Db} sites in dickite. Here again and for the same reason, a systematical shift is observed between the maximum of the distribution and the Fe_D parameters along an axis of constant rhombicity ($\lambda_D = B_2^2/B_2^0 \approx 0.8$). Note that the shifts are in opposite directions for the $Fe_{(II)}$ and Fe_D sites because the specific positions of the related lines of these sites for the X and Q-band constrain the distribution calculation differently. The third

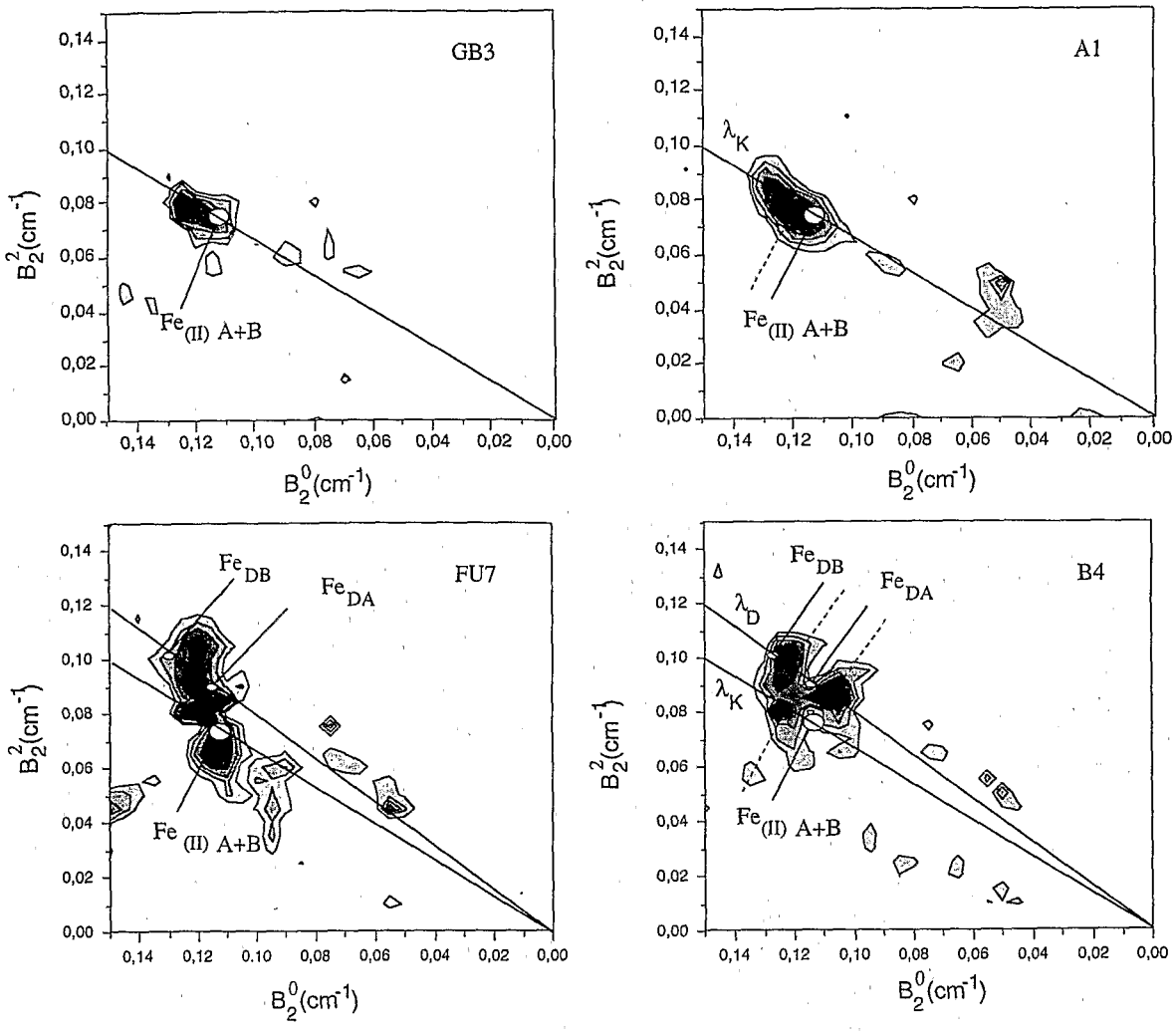

Figure 8. Calculated distribution of the fine-structure parameters for the GB3, A1, FU7, and B4 kaolinites. Highly ordered GB3 and A1 kaolinites are characterized by only one distribution mode around the $Fe_{(II)}$ fine-structure parameters whereas the poorly ordered FU7 and B4 kaolinites exhibit two additional distribution modes, corresponding to the two distinct fine-structure parameter sets calculated for the Fe_{Da} and Fe_{Db} sites in dickite. Note the systematic shifts along axes of constant rhombicity (λ_K and λ_D) observed between the maxima of the distribution and the reference parameters.

mode is close to the parameters calculated for $Fe_{(II)}$ sites in well-ordered kaolinite. For the FU7 sample, these three modes can also be recognized, although they are less pronounced. An additional mode is observed around $B_2^0 = 0.11$ cm^{-1} and $B_2^2 = 0.065$ cm^{-1} for this sample. This mode does not contribute to the $Fe_{(I)}$ signal, but it is related to axial contributions observed on the X-band spectrum, *i.e.*, the outer tails of the broadened 340 $Fe_{(II)}$ lines.

DISCUSSION

Structural Fe^{3+} in well-ordered samples

Kaolinite. Although the superposition model (SPM) (Newman and Urban, 1975) does not always give convincing results (Lehmann, 1980), it was tentatively used to interpret the fine-structure parameters of Fe^{3+} in kaolinite. In this model, it is assumed that the fine-structure parameters for a cation can be assessed by a sum of axially symmetric contributions of the surrounding ligands. For kaolinite, SPM calculations were performed using the atomic positions around Al^{3+} determined by Rietveld refinement on XRD and neutron-diffraction data at room temperature (Bish and Von Dreele, 1989) and at 1.5 K (Bish, 1993) on the Keokuk kaolinite. SPM calculations were performed in the reference frame a^*bc'. c' is orthogonal to a^*b and is thus nearly collinear to c. The second-order principal axis Z_2 lies close to the [001] direction ((Z_2, c) < 30°) for both Al1 and Al2 sites at both temperatures. This orientation is consistent with the orienta-

tion of the Z axis assessed experimentally by Meads and Malden (1975) on oriented kaolinite samples. In addition, for both Al sites, the decrease of the calculated B^0_{2SPM} value as a function of increasing temperature is in relative agreement with the variation of the observed B^0_2 values determined here. This decrease is due to the stretching of the structure along the *c* axis (Bish, 1993) and is consistent with the Fe^{3+} substitution for Al^{3+} in Al1 and Al2 sites of kaolinite. The three-fold pseudo-symmetry axis Z_3 (Gaite and Rager, 1997) also lies close to the crystallographic *c* axis for both Al-sites ($(Z_3, c) < 16°$). The near coincidence between the Z_2 and Z_3 axis directions ($(Z_3, Z_2) < 15°$) may explain why the experimental B^3_4 and B^{-3}_4 values, refined in the second-order principal-axis frame, have highest values among the fourth-order parameters for both $Fe_{(II)}$ sites.

Dickite. The occurrence of two Fe^{3+} centers in dickite is in agreement with the existence of two non-equivalent crystallographic Al^{3+} sites in the dickite structure (Bish and Johnston, 1993). A decrease in the determined B^0_2 value is observed for both Fe^{3+} centers as a function of increasing temperature, and this decrease is of the same magnitude as that observed for $Fe_{(II)}$ sites in kaolinite (Figure 5). Hence, the EPR signals for Fe^{3+} in dickite correspond to Fe^{3+} substitutions for Al^{3+} in the two Al sites of the dioctahedral layer.

Structural Fe^{3+} in poorly ordered kaolinites

According to Bookin *et al.* (1989), adjacent 1:1 layers in ordered kaolinite are shifted by $-a/3$ and the vacancy corresponds to the B site of the dioctahedral sheet (B-layer). In contrast, the vacancy in the monoclinic two-layer structure of dickite alternates between the B and C sites to produce a regular alternation of B and C-layers. Note that the real structure of the kaolinite B-layer differs from that of the dickite B-layer. Until now, disorder in kaolinites has been mainly explained using models based on the combination of various defects, such as stacking faults related to layer rotation ($\pm 120°$) or layer translation ($\pm b/3$ shift), occurrence of enantiomorphic layers, or vacancy displacement (*e.g.*, Giese, 1988; Bookin *et al.*, 1989). Plançon *et al.* (1989) proposed a model based mainly on translations of B-layers with a minor contribution from vacancy displacement. A continuum from the kaolinite structure to the dickite structure was also suggested from infra-red spectroscopy (Brindley *et al.*, 1986). In such a continuum, the disordered kaolinite may correspond to an intermediate state between a well-ordered kaolinite and a well-ordered dickite.

The match between two distinct modes of the distribution of the fine-structure parameters for FU7 and B4 samples and the parameters of the Fe_{Da} and Fe_{Db} sites of dickite demonstrates unambiguously the occurrence of layers possessing a dickite 1:1 layer structure interstratified with kaolinite layers. As clearly demonstrated by Prost *et al.* (1989), a dickite-like hydroxyl configuration occurs in the disordered kaolinite structure. Moreover, the model for the disordered kaolinite structure proposed by Artioli *et al.* (1995), based on XRD modeling and electrostatic calculations, combines the random occurrence of triclinic B and C-layers with their enantiomorphic layers.

The EPR results presented here indicate the existence of Fe^{3+} sites with symmetry intermediate between that of $Fe_{(II)}$ and Fe_D sites and suggest a continuous change of Fe^{3+} site symmetry from that of the Fe sites in the ordered B-B kaolinite stacking ($Fe_{(II)}$ sites) to that of the Fe sites in the ordered B-C dickite stacking (Fe_D sites). As the fine-structure parameters are primarily sensitive to the symmetry of the first coordination shell, this suggests a structural change of the intercalated C-layer and of the adjacent B-layers towards the structure of dickite C and B-layers, respectively. This distortion would probably depend on the length of the dickite-type sequence. We emphasize the assumption of Plançon *et al.* (1989) that "the occurrences of C-layers among B-layers probably induces a distortion of the layer structures so that they are more similar". Consequently, the occurrence of a continuous distribution of fine-structure parameters for the most disordered samples supports the hypothesis of random intercalation of C-layers among kaolinite B-layers, giving the observed $Fe_{(I)}$ signal, rather than a sum of dickite and kaolinite EPR spectra.

Hence, when long range disorder prevails over local perturbations, the occurrence of an $Fe_{(I)}$ signal on the X-band EPR spectra of poorly ordered kaolinites is a diagnostic feature for the occurrence of C-layers in the kaolinite structure.

ACKNOWLEDGMENTS

The authors are indebted to S.S. Hafner (University of Marburg, Germany) for the access to the 4K EPR measurement facility and to N. Petit (ENSMP, Paris) for help with the E04NAF use. We thank J.-M. Gaite, B.A. Goodman, and S. Guggenheim for helpful and constructive reviews. This work was supported by the CNRS / INSU program "Géomatériaux". This is contribution INSU N° 177 and IPGP N° 1592.

REFERENCES

Abragam, A. and Bleaney, B. (1970) *Electron Paramagnetic Resonance of Transition Ions.* Clarendon Press, Oxford, 911 pp.

Allard, T. and Muller, J.-P. (1998) Kaolinite as an in situ dosimeter for past radionuclide migration at the Earth's surface. *Applied Geochemistry*, **13,** 751–765.

Angel, B.R. and Vincent, W.E.J. (1978) Electron spin resonance studies of iron oxides associated with the surface of kaolins. *Clays and Clay Minerals*, **26,** 263–272.

Artioli, G., Bellotto, M., Gualtieri, A., and Pavese, A. (1995) Nature of structural disorder in natural kaolinites: A new model based on computer simulation of powder diffraction data and electrostatic energy calculation. *Clays and Clay Minerals*, **43,** 438–445.

Bish, D.L. (1993) Rietveld refinement of the kaolinite structure at 1.5 K. *Clays and Clay Minerals*, **41,** 738–744.

Bish, D.L. and Johnston, C.T. (1993) Rietveld refinement and Fourier-transform infrared spectroscopy study of the dickite structure at low temperature. *Clays and Clay Minerals*, **41,** 297–304.

Bish, D.L. and Von Dreele. R.B. (1989) Rietveld refinement of non-hydrogen atomic positions in kaolinite. *Clays and Clay Minerals*, **37,** 289–296.

Bonnin, D., Muller, S., and Calas, G. (1982) Le fer dans les kaolins. Etude par spectrométries RPE, Mössbauer, EXAFS. *Bulletin de Minéralogie*, **105,** 467–475.

Bookin, A.S., Drits, V.A., Plançon, A., and Tchoubar, C. (1989) Stacking faults in kaolin-group minerals in the light of real structural features. *Clays and Clay Minerals*, **37,** 297–307.

Brindley, G.W., Kao, C.-C., Harrison, J.L., Lipsicas, M., and Raythatha, R. (1986) Relation between structural disorder and other characteristics of kaolinites and dickites. *Clays and Clay Minerals*, **34,** 239–249.

Buckmaster, H.A. (1962) Tables of matrix elements for the operators $O_2^{\pm 1}$, $O_4^{\pm 1}$, $O_6^{\pm 1}$, $O_6^{\pm 5}$. *Canadian Journal of Physics*, **40,** 1670–1677.

Cases, J-M., Liétard, O., Yvon, J., and Delon, J-F. (1982) Etude des propriétés cristallochimiques, morphologiques, superficielles de kaolinites désordonnées. *Bulletin de Minéralogie*, **105,** 439–455.

Clozel, B., Allard, Th., and Muller, J-P. (1994) Nature and stability of radiation induced defects in natural kaolinites: New results and a reapraisal of published works. *Clays and Clay Minerals*, **46,** 657–666.

Gaite, J-M. and Rager, H. (1997) Electron paramagnetic resonance study of Fe^{3+} at M_1 position in forsterite. *Journal of Physics: Condensed Matter*, **9,** 10033–10039.

Gaite, J-M., Ermakoff, P., and Muller, J-P. (1993) Characterization and origin of two Fe^{3+} EPR spectra in kaolinite. *Physics and Chemistry of Minerals*, **20,** 242–247.

Gaite, J-M., Ermakoff, P., Allard, Th., and Muller, J-P. (1997) Paramagnetic Fe^{3+}: A sensitive probe for disorder in kaolinite. *Clays and Clay Minerals*, **45,** 496–505.

Giese, R.F., Jr (1988) Kaolin minerals: Structures and stabilities. In *Hydrous Phyllosilicates (Exclusive of Micas), Reviews in Mineralogy, Volume 19*, S.W. Bailey, ed., Mineralogical Society of America, 29–66.

Goodman, B.A. and Hall, P.L. (1994) Electron paramagnetic spectroscopy. In *Clay Mineralogy: Spectroscopic and Chemical Determinative Methods*, M.J. Wilson, ed., Chapman & Hall, London, 173–225.

Hall, P.L. (1980) The application of electron spin resonance spectroscopy to studies of clay minerals: I. Isomorphous substitutions and external surface properties. *Clay Minerals*, **15,** 321–335.

Herbillon, A.J., Mestdagh, M.M., Vilelvoye, L., and Derouane, E.G. (1976) Iron in kaolinite with special reference to kaolinite from tropical soils. *Clay Minerals*, **11,** 201–220.

Kliava, J. (1986) EPR of impurity ions in disordered solids. *Physica Status Solidi B*, **134,** 411–455.

Legein, C., Buzare, J.Y., Emery, J., and Jacoboni, C. (1995) Electron paramagnetic resonance determination of the local field distribution acting on Cr^{3+} and Fe^{3+} in transition metal fluoride glasses (TMFG). *Journal of Physics: Condensed Matter*, **7,** 3853–3862.

Lehmann, G. (1980) Correlation of zero-field splittings and site distorsions II. Application of the superposition model to Mn^{2+} and Fe^{3+}. *Physica Status Solidi B*, **99,** 623–633.

Levitz, P., Bonnin, D., Calas, G., and Legrand, A.P. (1980) A two-parameter distribution analysis of Mössbauer spectra in non-crystalline solids using general inversion method. *Journal of Physics E: Scientific Instruments*, **13,** 427–432.

Lucas, Y., Chauvel, A., and Ambrosi, J.P. (1987) Processes of aluminium and iron accumulation in latosols developed on quartz rich sediments from central Amazonia (Manaus, Brazil). In *Proceedings of the International Meeting on Geochemistry of the Earth Surface and Processes of Mineral formation, Granada, Spain*, R. Rodriguez-Clemente and Y. Tardy, eds., Madrid: Consejo Superior de Investigaciones Cientificas, [Paris]: Centre national de la recherche scientifique, 289–299.

Malengreau, N., Muller, J.-P., and Calas, G. (1994) Fe-speciation in kaolins: A diffuse reflectance study. *Clays and Clay Minerals*, **42,** 137–147.

Meads, R.E. and Malden, P.J. (1975) Electron spin resonance in natural kaolinites containing Fe^{3+} and other transition metal ions. *Clay Minerals*, **10,** 313–345.

Mehra, O.P. and Jackson, M.L. (1960) Fe oxide removal from soil and clays by a dithionite-citrate system buffered with sodium carbonate. *Clays and Clay Minerals*, **7,** 317–327.

Mestdagh, M.M., Herbillon, A.J., Rodrigue, L., and Rouxhet, P.G. (1982) Evaluation du rôle du fer structural sur la cristallinité des kaolinites. *Bulletin de Minéralogie*, **105,** 457–466.

Morin, G. and Bonnin, D. (1999) Modeling EPR powder spectra using numerical diagonalization of the spin Hamiltonian. *Journal of Magnetic Resonance*, **136,** 176–199.

Muller, J.-P. and Bocquier, G. (1987) Textural and mineralogical relationships between ferruginous nodules and surrounding clayey matrices in a laterite from Cameroon. In *Proceedings of the International Clay Conference, Denver, 1985*, L.G. Schultz, H. Van Olphen, and F.A. Mumpton, eds., The Clay Minerals Society, Bloomington, Indiana, 186–196.

Muller, J.-P. and Calas, G. (1989) Tracing kaolinites through their defect centers. Kaolinite paragenesis in a laterite (Cameroon). *Economic Geology*, **84,** 694–707.

Muller, J.-P. and Calas, G. (1993) Genetic significance of paramagnetic centers in kaolinites In *Kaolin Genesis and Utilization*, H.H. Murray, W. Bundy and C. Harvey, eds., The Clay Minerals Society, Boulder, 341 pp.

Muller, J.-P., Manceau, A., Calas, G., Allard, T., Ildefonse, P., and Hazemann, J-L. (1995) Crystal-chemistry of kaolinite and Fe-Mn oxides: Relation with formation conditions of low-temperature systems. *American Journal of Science*, **295,** 115–1155.

Murray, H.H. (1988) Kaolin minerals: Their genesis and occurrences. In *Hydrous Phyllosilicates (Exclusive of Micas), Reviews in Mineralogy, Volume 19*, S.W. Bailey, ed., Mineralogical Society of America, 67–89.

Newman, D.J. and Urban, W. (1975) Interpretation of S-state ion spectra. *Advances in Physics*, **24,** 793–844.

Plançon, A., Giese, R.F., Snyder, R., Drits, V.A., and Bookin, A.S. (1989) Stacking faults in the kaolin-group minerals: The defect structure of kaolinite. *Clays and Clay Minerals*, **37,** 203–210.

Prost, R., Damene, A., Huard, E., Driard, J., and Leydecker, J.P. (1989) Infrared study of structural OH in kaolinite, dickite, nacrite and poorly crystalline kaolinite at 5 to 600 K. *Clays and Clay Minerals*, **37,** 464–468.

Rudowicz, C. (1985) Transformation relations for the conventional O_q^k and normalized O_q^k Stevens operator equivalents with $k = 1$ to 6 and $-k \leq q \leq k$. *Journal of Physics C: Solid State Physics*, **18,** 1415–1430.

(Received 19 May 1998; accepted 2 April 1999; Ms. 98-063)